Environmental Science & Technology

Article

pubs.acs.org/est

# Molecular Simulation of Carbon Dioxide, Brine, and Clay Mineral Interactions and Determination of Contact Angles

Craig M. Tenney* and Randall T. Cygan

Sandia National Laboratories, 1515 Eubank, Albuquerque, New Mexico 87123, United States

Supporting Information

**ABSTRACT:** Capture and subsequent geologic storage of $CO_2$ in deep brine reservoirs plays a significant role in plans to reduce atmospheric carbon emission and resulting global climate change. The interaction of $CO_2$ and brine species with mineral surfaces controls the ultimate fate of injected $CO_2$ at the nanoscale via geochemistry, at the pore-scale via capillary trapping, and at the field-scale via relative permeability. We used large-scale molecular dynamics simulations to study the behavior of supercritical $CO_2$ and aqueous fluids on both the hydrophilic and hydrophobic basal surfaces of kaolinite, a common clay mineral. In the presence of a bulk aqueous phase, supercritical $CO_2$ forms a nonwetting droplet above the hydrophilic surface of kaolinite. This $CO_2$ droplet is separated from the mineral surface by distinct layers of water, which prevent the $CO_2$ droplet from interacting directly with the mineral surface. Conversely, both $CO_2$ and $H_2O$ molecules interact directly with the hydrophobic surface of kaolinite. In the presence of bulk supercritical $CO_2$, nonwetting aqueous droplets interact with the hydrophobic surface of kaolinite via a mixture of adsorbed $CO_2$ and $H_2O$ molecules. Because nucleation and precipitation of minerals should depend strongly on the local distribution of $CO_2$, $H_2O$, and ion species, these nanoscale surface interactions are expected to influence long-term mineralization of injected carbon dioxide.

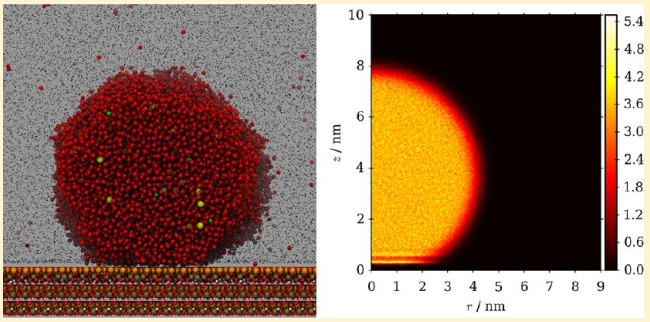


## INTRODUCTION

Capture and subsequent geologic storage of $CO_2$ in deep brine reservoirs plays a significant role in plans to reduce atmospheric carbon emission and resulting global climate change.[1] Evaluation and implementation of proposed scenarios for injecting $CO_2$ into sedimentary reservoirs requires understanding the interactions between supercritical $CO_2$, aqueous brines, and the mineral phases found in the reservoir and overlying caprock. In particular the relative wetting of pore surfaces in the rock matrix by $CO_2$ and brine, characterized macroscopically by contact angles, controls the capillary pressure of the fluids in the pore and strongly influences the transport and ultimate distribution of $CO_2$ in the reservoir.[2,3] Knowledge of molecular interactions between fluid and mineral phases can be used to develop larger-scale conceptual models for multiphase surface wetting to help evaluate the fate of supercritical $CO_2$ in the reservoir.[4,5]

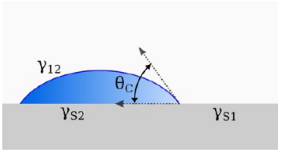


**Figure 1.** Contact angle $\theta_C$ resulting from the balance of forces between interfacial tensions $\gamma_{ij}$ between two fluids (subscripts 1 and 2) and a solid surface (subscript S).

A contact angle $\theta_C$ is defined here as the angle formed between the interface of a droplet and solid surface and the interface of the droplet and the surrounding bulk fluid phase (see Figure 1). For wetting fluids $\theta_C < \pi/2$ and for nonwetting fluids $\theta_C > \pi/2$. As described by Young's equation,

$$\gamma_{S1} = \gamma_{S2} + \gamma_{12}\cos\theta_C \quad (1)$$

the equilibrium contact angle results from the balance of forces between the interfacial tensions (or surface free energies) $\gamma_{ij}$ between two fluids (subscripts 1 and 2) and a solid surface (subscript S). Note that this definition and eq 1 only truly apply to macroscopic systems, and complications may arise when contact angle is considered at the nanoscale. For example, as droplet size decreases, the free energy associated with creating the three-phase contact line may become significant and needs to be added to eq 1.[6−8] Also, near the three-phase line molecular interactions between two phases can be altered by the presence of the third phase, resulting in a local nanoscale contact angle that may differ from its macroscopic value. While the work described in this paper is primarily concerned with

Received: September 24, 2013
Revised: December 2, 2013
Accepted: January 10, 2014
Published: January 10, 2014

   dx.doi.org/10.1021/es404075k | Environ. Sci. Technol. 2014, 48, 2035−2042

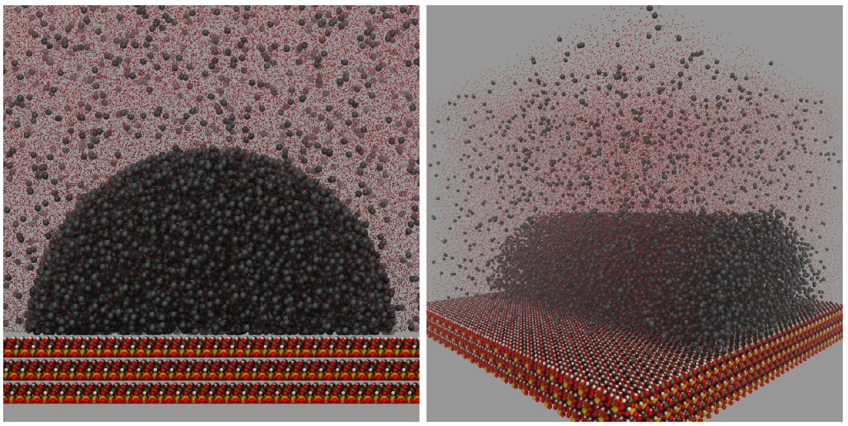

(a) Front view (b) Oblique view

**Figure 2.** Initial configuration of an infinitely long $CO_2$ "droplet" on the gibbsite surface of kaolinite in the presence of water containing dissolved $CO_2$. Aluminum, silicon, oxygen, and hydrogen atoms within the kaolinite slab are represented as brown, yellow, red, and white spheres, respectively. Above the kaolinite slab black spheres are $CO_2$ carbon atoms and red dots are $H_2O$ oxygen atoms. Atoms represented as spheres are rendered at 60% of their van der Waals radius.

general wetting trends and details of molecular ordering at interfaces, we attempted to minimize the potential for nano- versus macro-scale complications by simulating relatively large systems with cylindrical, as opposed to spherical, droplet geometries. The systems used in this study are described in greater detail in the next section. For the purposes this paper, we will generally assume an interpretation of contact angle akin to that depicted in Figure 1.

In addition to influencing relative flows of $CO_2$ and brine during both injection and postinjection periods, interfacial tension and wetting behavior also determine the potential $CO_2$ storage capacity of a reservoir.[9,10] The Young−Laplace equation

$$P_C = \gamma_{12}\frac{2\cos\theta_C}{r} \quad (2)$$

describes the capillary pressure $P_C$ across the interface of two fluids as a function of the surface tension $\gamma_{12}$, contact angle $\theta_C$, and effective capillary (or pore) radius $r$. Each potential leakage pathway through the caprock has a minimum effective capillary radius, or tightest restriction, at some point along the path. As more $CO_2$ is injected, pressure exerted on the reservoir caprock by the buoyant $CO_2$ increases. Leakage will occur when the pressure due to buoyancy exceeds the capillary pressure of the pathway with the least restriction to flow. This critical capillary pressure is calculated from eq 2 using the minimum effective capillary radius of this flow path with the least restriction.

Experimental studies have been conducted to determine the wettability of caprock and reservoir materials in $CO_2$−brine systems,[11−16] but reported wetting trends with respect to temperature, pressure, and brine composition are not always consistent.[17,18] The main objective of this research is to provide nanoscale resolution of interactions at fluid−fluid and fluid−solid interfaces through molecular simulation to clarify some of the issues behind conflicting experimental results. Previous studies of contact angles using molecular simulation include water on graphene,[19−21] water and surfactant on hydrocarbon surfaces,[22] water on gold,[23] epoxy on $SiO_2$,[24] $CO_2$ and brine on quartz,[25] and water on kaolinite.[26] Molecular simulation has also been used to study interfacial tension in $CO_2$−water systems.[27,28]

In this study we used molecular dynamics simulations[29,30] to investigate interfacial behavior and evaluate contact angles for $CO_2$-brine-mineral systems. Accurate interatomic potentials[31,32] were used to evaluate the energy and forces associated with hundreds of thousands of atoms for various fluid droplet configurations on the basal surfaces of kaolinite, a common clay mineral. Clay minerals are present in many potential sites being considered for carbon sequestration, where the clay phases occur as coatings on sandstone grains and as the dominant mineral phase of shale caprocks. Some clay phases provide relatively uniform basal surfaces that are suitable for experimental determinations of contact angles. Kaolinite is characterized by both hydrophilic and hydrophobic basal surfaces, which allows investigation of contrasting wetting behavior for $CO_2$ and aqueous phases that would exist in the reservoir. Although recent experimental evidence has shown that supercritical $CO_2$ intercalates and expands low-charge smectite minerals such as montmorillonite,[33−35] kaolinite does not appear to swell with $CO_2$ at such conditions. In addition to providing the foundational science for understanding the molecular control in wetting processes, such results can be used to improve capillary flow and capillary trapping models to better assess the disposition of $CO_2$ in sequestration reservoirs.

## SIMULATION DETAILS

Kaolinite was chosen as the model mineral surface for this study because it provides a relatively simple substrate for studying surface adsorption, due to its lack of interlayer mineral sites and the presence of both hydrophilic and hydrophobic basal surfaces. Kaolinite[36−39] ($Al_2Si_2O_5(OH)_4$) is a 1:1 layer clay wherein each layer is made up of an $AlO_6$ octahedral sheet and a $SiO_4$ tetrahedral sheet. Figure S1 in the Supporting Information shows the structure for a kaolinite unit cell. Throughout this paper the octahedral sheet will be referred to as the gibbsite surface, and the tetrahedral sheet as the siloxane surface. The basal siloxane surface is relatively hydrophobic, while the basal gibbsite surface is quite hydrophilic and capable of significant hydrogen bonding.[26] Layers are held together by hydrogen bonds between hydroxyl groups extending from the gibbsite surface of one layer to the basal oxygens on the siloxane surface of the next layer. The systems studied in this work focus solely upon the basal surfaces of kaolinite. Carbon

**Table 1. $CO_2$-Brine-Mineral Simulation Systems Referred to in This Study**

| | number of molecules | | | |
|---|---|---|---|---|
| | $CO_2$ | $H_2O$ | NaCl | $CaCl_2$ |
| Kaolinite Gibbsite Surface | | | | |
| $CO_2$ droplet in $H_2O$ | 15 000 | 130 000 | | |
| $CO_2$ droplet in 0.78 M NaCl | 14 000 | 118 000 | 1650 | |
| $CO_2$ droplet in 0.26 M $CaCl_2$ | 14 000 | 118 000 | | 550 |
| Kaolinite Siloxane Surface | | | | |
| $CO_2$ droplet in $H_2O$ | 7000 | 150 000 | | |
| $CO_2$ droplet in 0.78 M NaCl | 7000 | 150 000 | 2100 | |
| $CO_2$ droplet in 0.26 M $CaCl_2$ | 7000 | 150 000 | | 700 |
| $H_2O$ droplet in $CO_2$ | 52 000 | 32 000 | | |
| 0.78 M NaCl droplet in $CO_2$ | 40 000 | 32 000 | 450 | |
| 0.26 M $CaCl_2$ droplet in $CO_2$ | 40 000 | 32 000 | | 150 |

dioxide is expected to be more reactive at kaolinite edges, where protonation−deprotonation reactions with the brine or $CO_2$ fluid can control reactions with the clay. While it is known that charge density on the basal surfaces of kaolinite can vary with pH,[40] we did not attempt to explicitly account for this, and instead allowed the initial, experimentally derived crystal structure[41] to relax and adsorb fluid species as dictated by the simulation force field.

Figure 2 shows the initial configuration used for the simulation of a $CO_2$ droplet in contact with the gibbsite surface of kaolinite in an environment of water and dissolved $CO_2$. The simulation cell contains a three-layer slab of kaolinite (approximately 2 nm thick) with fluid located adjacent to the gibbsite surface. For the half-cylinder droplet shown in Figure 2, periodic boundary conditions result in an infinitely long droplet or filament. Cylindrical droplet geometries have been used previously for determination of contact angle via molecular simulation and study of the effects of the three-phase line tension.[21] A cylindrical droplet geometry was chosen in favor of conventional spherical geometry to reduce two potential scale effects. First, use of cylindrical geometry reduces droplet curvature, which reduces the pressure differential across the liquid−liquid interface of these nanoscale droplets (eq 2), which improves the match between nano- and macroscale pressures interior to the droplet. Second, use of cylindrical geometry eliminates the influence of the three-phase line tension, which can significantly influence contact angle results at small length scales.[6−8] Previous simulations using spherical droplets (not shown) showed no preferential wetting direction on either basal surface of kaolinite, and the effect of different orientations of the cylindrical droplet axis was not explored.

Similar initial configurations were used for most of the systems described in this paper. These other systems may include the use of NaCl or $CaCl_2$ brines instead of pure water, an aqueous droplet surrounded by $CO_2$ instead of $CO_2$ surrounded by water, or the siloxane surface instead of gibbsite. Table 1 summarizes the $CO_2$-brine-mineral simulation systems referred to in this paper. $Na^+$, $Ca^{2+}$, and $Cl^-$ are the most common ionic constituents found in deep brine reservoirs of interest for $CO_2$ sequestration.[42] Simplified NaCl and $CaCl_2$ brines were used in this study to isolate the behavior of monovalent and divalant cations. Brine compositions were chosen to result in approximately identical ionic strengths.

All systems were simulated at a temperature of 330 K and a pressure of 20 MPa, which is above the critical point for carbon dioxide and represents a realistic temperature and pressure for a deep saline aquifer. Further details regarding the methods and parameters used for simulation and analysis in this study can be found in the Supporting Information.

## RESULTS AND DISCUSSION

Figure 3a shows the final configuration of an infinitely long cylindrical supercritical $CO_2$ droplet interacting with the basal gibbsite surface of kaolinite in the presence of water and dissolved $CO_2$. Figure 4 shows the time- and space-averaged relative densities of $CO_2$ and $H_2O$ around the droplet for the same system. Figure 4b shows clearly that the $CO_2$ droplet is separated from the mineral surface by a thin, dense water layer (the bright, white line) at approximately $z$ = 0.15 nm and a second, much more diffuse water film located at approximately $z$ = 0.5 nm. Slightly enhanced mixing of $CO_2$ at the bottom of the droplet into the top of the diffuse water film at $z$ = 0.5 nm can be seen in Figure 4a. These observations suggest that the wetting behavior of $CO_2$ on the hydrophilic surface of kaolinite is strongly influenced by intervening water at the mineral surface.

Replacing water with brine in the simulation system reduces $CO_2$ wetting of the gibbsite surface of kaolinite. Figure 3b and c show supercritical $CO_2$ droplets floating freely above the gibbsite surface of kaolinite in the presence of $CaCl_2$ and NaCl brines, respectively. In contrast to the $CO_2$-water system shown in Figure 3a, which started from a similar initial configuration, $CO_2$ droplets in the presence of brine detached completely from the mineral surface. Figures 5 and 6 show the time- and space-averaged relative densities of $CO_2$, $H_2O$, and ions around

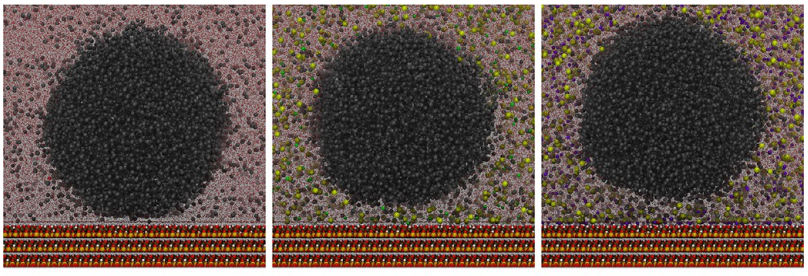


**Figure 3.** Snapshots of $CO_2$ droplets on the gibbsite surface of kaolinite in the presence of (a) water, (b) 0.26 M $CaCl_2$ brine, or (c) 0.78 M NaCl brine at 330 K and 20 MPa. Aluminum, silicon, oxygen, and hydrogen atoms within the kaolinite slab are represented as brown, yellow, red, and white spheres, respectively. Above the kaolinite slab black spheres are $CO_2$ carbon atoms; small red dots are $H_2O$ oxygen atoms; and yellow, green, and purple spheres are $Cl^-$ $Ca^{2+}$, and $Na^+$ ions, respectively. Atoms represented as spheres are rendered at 60% of their van der Waals radii.


dx.doi.org/10.1021/es404075k | Environ. Sci. Technol. 2014, 48, 2035−2042

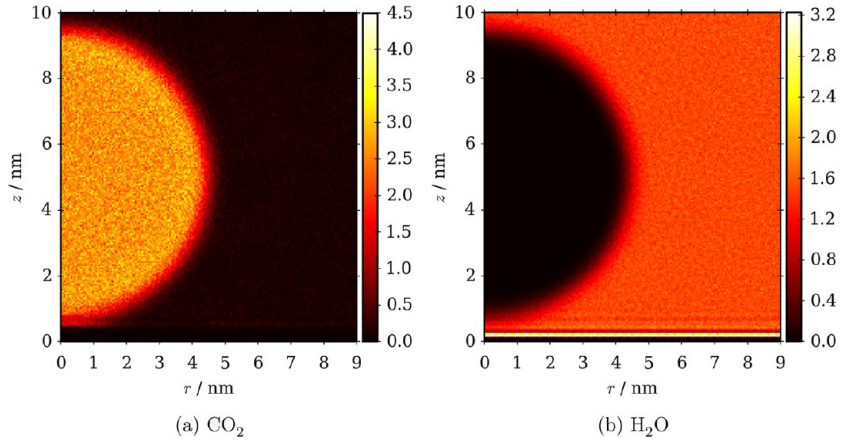


**Figure 4.** Relative density of $CO_2$ and $H_2O$ averaged over the final 2 ns of simulation around and along the plane of (approximate) system symmetry passing through the long axis of the $CO_2$ droplet on the gibbsite surface of kaolinite in the presence of water pictured in Figure 3a. Relative densities vary from 0 (black), through intermediate values (red to yellow), to the maximum value observed in the system (white). A relative density of 1 corresponds to the mean density of the indicated species within the simulation box. For the vertical axis $z$ = 0 nm corresponds to the initial $z$ position of the hydrogen atoms in the outer gibbsite surface of the kaolinite slab.

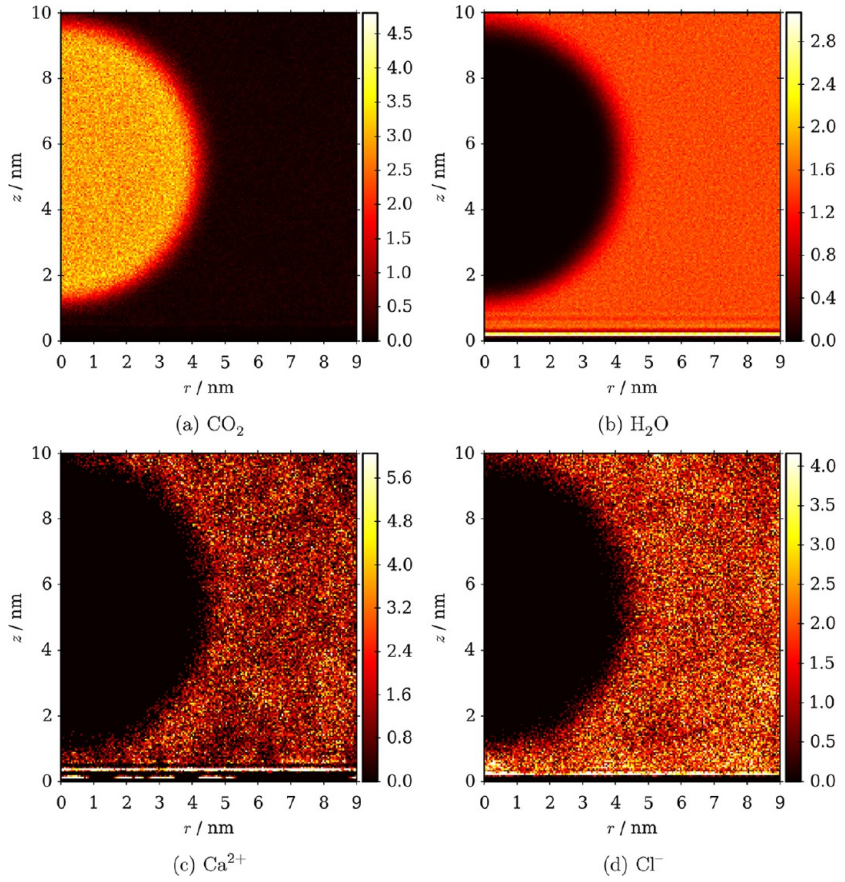


**Figure 5.** Relative density of various species for the $CO_2$ droplet on the gibbsite surface of kaolinite in the presence of $CaCl_2$ brine pictured in Figure 3b. Averaging methodology, color scales, and axes are as described for Figure 4

the $CO_2$ droplet for the $CaCl_2$ and NaCl brine-containing systems, respectively. Significant adsorption of water, cations, and anions at the mineral surface is evident. Figure 5c shows formation of a distinct layer of $Ca^{2+}$ interacting with the mineral surface through a layer of intermediate water molecules. The highest density of $Cl^-$ anions (Figure 5d) in this system occurs between the mineral surface and the layer of $Ca^{2+}$. This contrasts with the behavior seen in Figure 6c, where a distinct layer of $Na^+$ interacts directly with the mineral surface and $Cl^-$ density (Figure 6d) is highest just outside this $Na^+$ layer. The relative adsorption behavior of $Ca^{2+}$ and $Na^+$ is consistent with their hydration energies, where the divalent cation prefers coordination by water molecules, rather than adsorbing directly to the surface as $Na^+$ does in these simulations. Figures 5a and 6a show no association of $CO_2$ with the mineral surface or water/ion layers just above the mineral surface. This contrasts


dx.doi.org/10.1021/es404075k | Environ. Sci. Technol. 2014, 48, 2035−2042

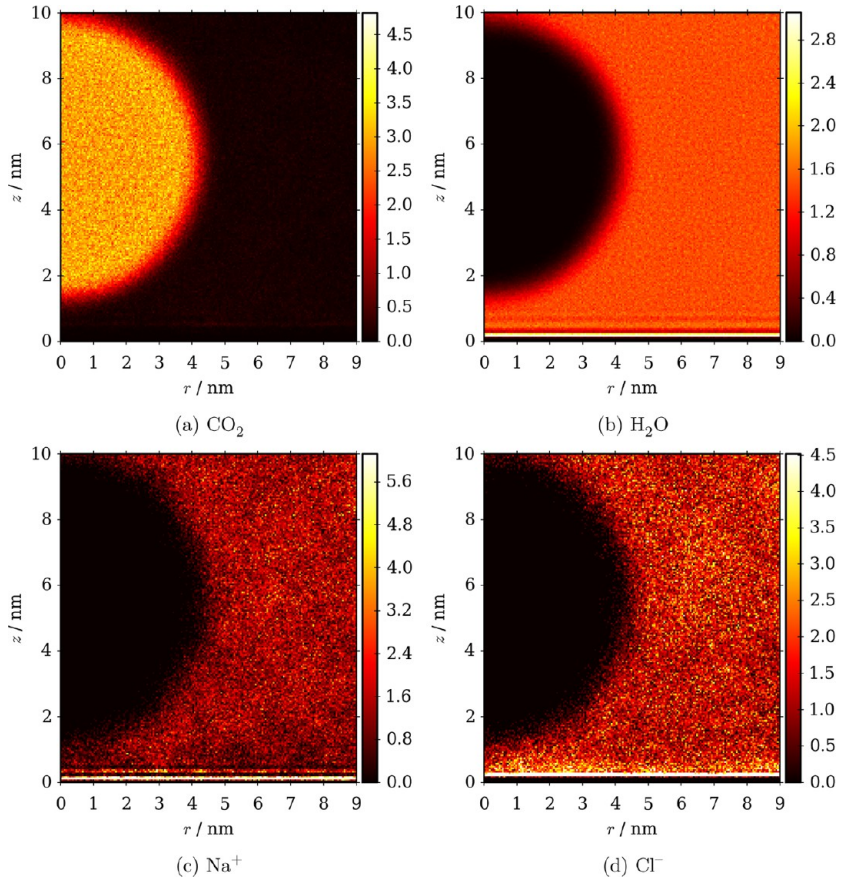


**Figure 6.** Relative density of various species for the $CO_2$ droplet on the gibbsite surface of kaolinite in the presence of NaCl brine pictured in Figure 3c. Averaging methodology, color scales, and axes are as described for Figure 4

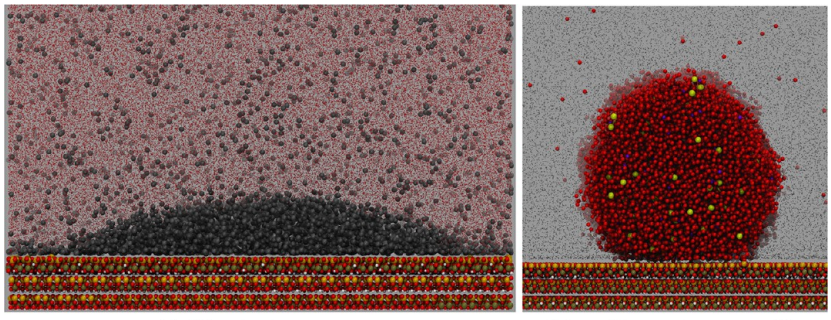


**Figure 7.** Droplets on the siloxane surface of kaolinite at 330 K and 20 MPa. (a) $CO_2$ droplet in the presence of water. Above the kaolinite slab, black spheres are $CO_2$ carbon atoms and red dots are $H_2O$ oxygen atoms. (b) NaCl brine droplet in the presence of $CO_2$. Above the kaolinite slab black dots are $CO_2$ carbon atoms, red spheres are $H_2O$ oxygen atoms, yellow spheres are $Cl^-$, and purple spheres are $Na^+$. For both figures aluminum, silicon, oxygen, and hydrogen atoms within the kaolinite slab are represented as brown, yellow, red, and white spheres, respectively. Atoms represented as spheres are rendered at 60% of their van der Waals radii.

with observations from Figure 4a, which showed slightly enhanced mixing of $CO_2$ from the droplet with the diffuse water layer just above the mineral surface. The reduced interaction and resulting detachment of the $CO_2$ droplet from the surface may be due to the lower solubility of $CO_2$ in brine, an effect which may be further enhanced near the mineral surface due to the increased presence and ordering of ions.

Simulations of water or brine droplets on the gibbsite surface of kaolinite in the presence of $CO_2$ all resulted in essentially complete wetting of the surface by the aqueous phase and are not shown. As required by eq 1, (nearly) complete wetting of the surface by the aqueous phase is consistent with (nearly) complete nonwetting of the surface by the $CO_2$ phase, which is the behavior described above.

Figure 7a shows the final configuration of a supercritical $CO_2$ droplet interacting with the siloxane surface of kaolinite in the presence of water. The droplet geometry indicates strong wetting of the siloxane surface by $CO_2$. Similar systems using brine instead of water displayed similar behavior and are not shown. Unlike other systems described in this paper, the initial configuration for this system was a hemisphere of $CO_2$ on the outer siloxane surface of the kaolinite slab, rather than an


dx.doi.org/10.1021/es404075k | Environ. Sci. Technol. 2014, 48, 2035−2042

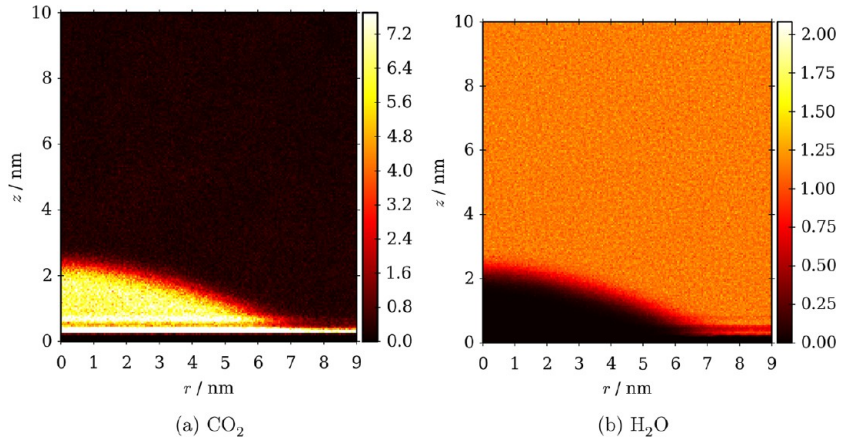


**Figure 8.** Relative density of $CO_2$ and $H_2O$ averaged around and along the plane of (approximate) system symmetry passing through the long axis of the $CO_2$ droplet in Figure 7a for the final 2 ns of the simulation. Relative densities vary from 0 (black), through intermediate values (red to yellow), to the maximum value observed in the system (white). A relative density of 1 corresponds to the mean density of the indicated species within the simulation box. For the vertical axis $z$ = 0 nm corresponds to the initial $z$ position of the oxygen atoms in the outer siloxane surface of the kaolinite slab.

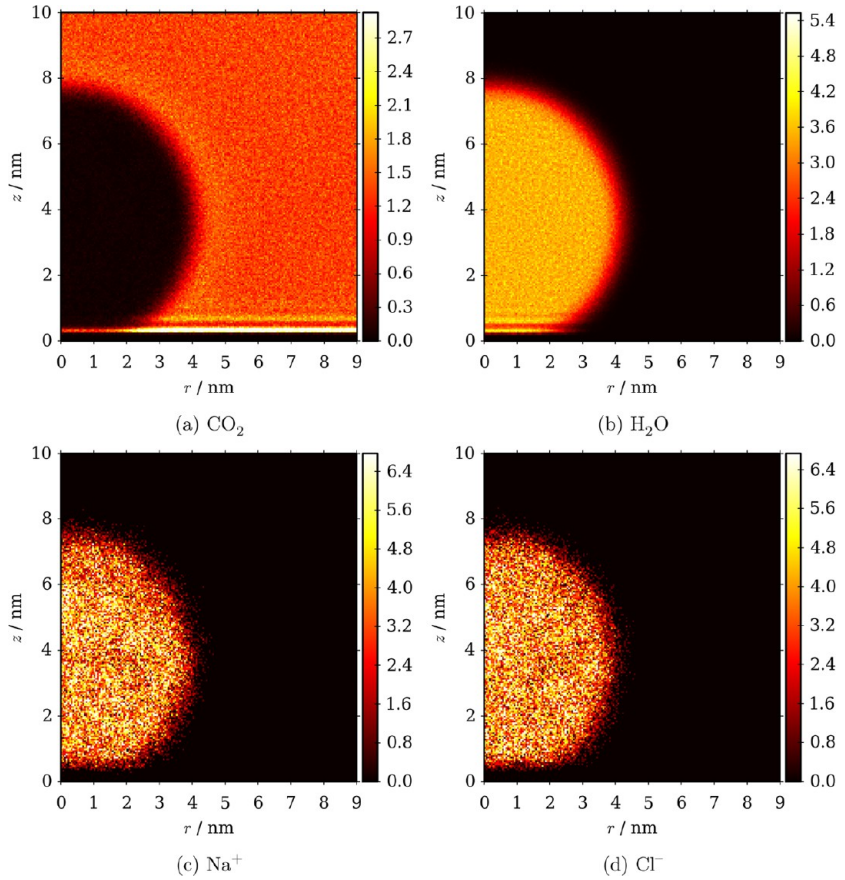


**Figure 9.** Relative density of various species for a NaCl brine droplet on the siloxane surface of kaolinite in the presence of supercritical $CO_2$. Averaging methodology, color scales, and axes are as described for Figure 8.

infinite half cylinder like that shown in Figure 2. Although the droplet started as a hemisphere, it spontaneously rearranged into the infinitely long mound of $CO_2$ pictured in Figure 7a. The evolution and long-term behavior of similar $CO_2$-on-siloxane systems with greater or lesser numbers of $CO_2$ molecules (not shown) were strongly dependent upon the number of $CO_2$ molecules present in the system. If too few $CO_2$ molecules were available, an isolated (i.e., finite) mound or scattered clusters of adsorbed $CO_2$ formed instead of an infinitely long mound. If too many $CO_2$ molecules were present, droplet edges interacted with periodic images of the droplet, and an infinite sheet of $CO_2$ formed over the entire siloxane surface. Figure 8 shows the time- and space-averaged relative density of $CO_2$ and $H_2O$ around the droplet for the system shown in Figure 7a. Figure 8a shows a distinct layer of $CO_2$ interacting directly with the entire siloxane surface. Under


dx.doi.org/10.1021/es404075k | Environ. Sci. Technol. 2014, 48, 2035−2042

**Table 2. Contact Angles at 330 K and 20 MPa Measured from Simulation Results.**[a]

| | aqueous phase | | |
|---|---|---|---|
| | $H_2O$ | 0.78 M NaCl | 0.26 M $CaCl_2$ |
| kaolinite gibbsite surface | | | |
| $CO_2$ droplet in aqueous phase | 169° ± 3° | 180° | 180° |
| aqueous droplet in $CO_2$ | – | – | – |
| kaolinite siloxane surface | | | |
| $CO_2$ droplet in aqueous phase | 31° ± 6° | 26° ± 6° | 34° ± 6° |
| aqueous droplet in $CO_2$ | 145° ± 3° | 141° ± 3° | 145° ± 3° |

[a]Uncertainties were estimated based upon measurement uncertainties of droplet dimensions. Systems for which a contact angle could not be determined are denoted by "–".

the droplet this $CO_2$ layer completely excludes water, as shown by Figure 8b. Above the $CO_2$ layer interacting directly with the mineral surface is a region of depleted $CO_2$ density, followed by a region of slightly enhanced $CO_2$ density, which forms the base of the droplet. Beyond the edge of the $CO_2$ droplet, $CO_2$ and $H_2O$ both interact directly with the siloxane surface. This contrasts with what is seen for gibbsite surfaces, where only $H_2O$ interacts directly with the mineral (cf. Figure 4)

Figure 7b shows a snapshot of a NaCl brine droplet interacting with the siloxane surface of kaolinite in the presence of supercritical $CO_2$. Similar systems using water or $CaCl_2$ brine instead of NaCl brine displayed essentially identical behavior and are not shown. Figure 9 shows the time- and space-averaged relative density of $CO_2$, $H_2O$, $Na^+$, and $Cl^-$ around the droplet for the NaCl brine system. Results for the $CaCl_2$ system were similar and are not shown. Many of the observations made previously in the discussion of $CO_2$ droplets on the siloxane surface of kaolinite (Figure 8) also apply to Figure 9. Specifically, there exists a distinct $CO_2$ layer that interacts directly with the entire mineral surface. The formation of a second high-density region of $CO_2$ approximately 0.5−1.0 nm above the mineral surface in the bulk $CO_2$ region is also apparent in Figure 9a. As seen previously in Figure 8 and again now in Figure 9a and b, both $H_2O$ and $CO_2$ interact directly with the siloxane surface when an aqueous phase, in this case the brine droplet, is present above the surface. Unlike the behavior of brines over the gibbsite surface of kaolinite (Figures 5 and 6), Figure 9c and d display no preferential ordering of ions relative to the siloxane surface. Instead, ions appear to be distributed uniformly throughout the aqueous droplet. Also unlike the case seen with the gibbsite surface, wetting behavior did not appear to be greatly altered when switching the aqueous phase from water to NaCl or $CaCl_2$ brines.

Table 2 summarizes the contact angles measured from simulations of the systems studied in this work. The gibbsite surface of kaolinite is very strongly water-wetting and the siloxane surface strongly $CO_2$-wetting. As required by theory (eq 1), contact angles observed for $CO_2$-on-siloxane systems are the 180° supplement of contact angles for the water- or brine-on-siloxane systems. The strong water-wetting behavior of the gibbsite surface of kaolinite prevented direct determination of aqueous phase contact angles for that surface, but based upon contact angles measured for $CO_2$ droplets on the gibbsite surface, aqueous droplet contact angles would be less than 10°.

Using the definition of contact angle depicted in Figure 1, experimental measurements of contact angles for carbon dioxide on kaolinite in the presence of water or brine are approximately 160° ± 5°,[4] indicating that kaolinite is water-wetting. Unlike the model kaolinite surfaces used in this simulation study, these experimental contact angles were not measured for either the gibbsite or siloxane basal surfaces. Instead, experimental results correspond to contact angles measured over macroscopic surfaces composed of a likely random distribution of micro- or nanoscale crystals, which could present a hydrophobic or hydrophilic face or edge to the fluid phase. Consequently, direct comparison of experimental and simulation contact angles on basal surfaces is not practical for kaolinite.

This work predicts that the nanoscale distribution of wetting and nonwetting species can differ signficantly for different mineral surfaces, in spite of similar macroscopic contact angles. Because nucleation and precipitation of carbonate minerals depend on the local distribution of $CO_2$, $H_2O$, and dissolved ion species, nanoscale surface interactions can influence mineralization of injected carbon. While mineral trapping is desired for secure sequestration of $CO_2$, precipitation and dissolution of minerals necessarily alter pore structure within the rock matrix, thereby influencing fluid transport. The long-term fate of $CO_2$ will ultimately be controlled by the mixing of the injected $CO_2$ with reservoir brine to achieve thermodynamic saturation. Reliably understanding, predicting, and controlling $CO_2$ sequestration will require accounting for complex, coupled mechanisms of reaction and transport over a wide range of time and length scales.

## ■ ASSOCIATED CONTENT

### Supporting Information

Additional simulation setup and analysis details, force field parameters, and example LAMMPS input scripts are included in the Supporting Information. This material is available free of charge via the Internet at http://pubs.acs.org/.

## ■ AUTHOR INFORMATION

### Corresponding Author

*Phone: 505-284-4466; fax: 505-844-7786; e-mail: cmtenne@sandia.gov.

### Notes

The authors declare no competing financial interest.

## ■ ACKNOWLEDGMENTS

Thanks go to Ian Bourg (Lawrence Berkeley National Laboratory) and Louise Criscenti (Sandia National Laboratories) for helpful discussions regarding the best simulation methods for the study of contact angle phenomena. This material is based upon work supported as part of the Center for Frontiers of Subsurface Energy Security, an Energy Frontier Research Center funded by the U.S. Department of Energy, Office of Science, Office of Basic Energy Sciences under Award Number DE-SC0001114. Sandia National Laboratories is a multiprogram laboratory managed and operated by Sandia Corporation, a wholly owned subsidiary of Lockheed Martin Corporation, for the U.S. Department of Energy's National Nuclear Security Administration under contract DE-AC04-94AL85000.

## REFERENCES


(1) Metz, B. *IPCC Special Report on Carbon Dioxide Capture and Storage*, Working Group III; Cambridge University Press for the Intergovernmental Panel on Climate Change, 2005.

(2) Saadatpoor, E.; Bryant, S.; Sepehrnoori, K. New trapping mechanism in carbon sequestration. *Transp. Porous Media* **2010**, *82*, 3−17.

(3) Krevor, S. C. M.; Pini, R.; Li, B.; Benson, S. M. Capillary heterogeneity trapping of $CO_2$ in a sandstone rock at reservoir conditions. *Geophys. Res. Lett.* **2011**, *38*, n/a−n/a.

(4) Wang, S. B.; Edwards, I. M.; Clarens, A. F. Wettability phenomena at the $CO_2$-brine-mineral interface: Implications for geologic carbon sequestration. *Environ. Sci. Technol.* **2013**, *47*, 234−241.

(5) Parmigiani, A.; Huber, C.; Bachmann, O.; Chopard, B. Pore-scale mass and reactant transport in multiphase porous media flows. *J. Fluid Mech.* **2011**, *686*, 40−76.

(6) Amirfazli, A.; Neumann, A. W. Status of the three-phase line tension. *Adv. Colloid Interface Sci.* **2004**, *110*, 121−141.

(7) Tadmor, R. Line energy, line tension and drop size. *Surf. Sci.* **2008**, *602*, L108−L111.

(8) Brinkmann, M.; Kierfeld, J.; Lipowsky, R. Stability of liquid channels or filaments in the presence of line tension. *J. Phys.: Condens. Matter* **2005**, *17*, 2349−2364.

(9) Li, Z.; Dong, M.; Li, S.; Huang, S. $CO_2$ sequestration in depleted oil and gas reservoirs—Caprock characterization and storage capacity. *Energy Convers. Manage.* **2006**, *47*, 1372−1382.

(10) Naylor, M.; Wilkinson, M.; Haszeldine, R. Calculation of $CO_2$ column heights in depleted gas fields from known pre-production gas column heights. *Mar. Pet. Geol.* **2011**, *28*, 1083−1093.

(11) Chiquet, P.; Daridon, J. L.; Broseta, D.; Thibeau, S. $CO_2$/water interfacial tensions under pressure and temperature conditions of $CO_2$ geological storage. *Energy Convers. Manage.* **2007**, *48*, 736−744.

(12) Chiquet, P.; Broseta, D.; Thibeau, S. Wettability alteration of caprock minerals by carbon dioxide. *Geofluids* **2007**, *7*, 112−122.

(13) Espinoza, D. N.; Santamarina, J. C. Water-$CO_2$-mineral systems: Interfacial tension, contact angle, and diffusion-implications to $CO_2$ geological storage. *Water Resour. Res.* **2010**, *46*, 10.

(14) Bikkina, P. K. Contact angle measurements of $CO_2$-water-quartz/calcite systems in the perspective of carbon sequestration. *Int. J. Greenhouse Gas Control* **2011**, *5*, 1259−1271.

(15) Kim, Y.; Wan, J. M.; Kneafsey, T. J.; Tokunaga, T. K. Dewetting of silica surfaces upon reactions with supercritical $CO_2$ and brine: Pore-scale studies in micromodels. *Environ. Sci. Technol.* **2012**, *46*, 4228−4235.

(16) Saraji, S.; Goual, L.; Piri, M.; Plancher, H. Wettability of supercritical carbon dioxide/water/quartz systems: Simultaneous measurement of contact angle and interfacial tension at reservoir conditions. *Langmuir* **2013**, *29*, 6856−6866.

(17) Heath, J. E.; Dewers, T. A.; McPherson, B.; Nemer, M. B.; Kotula, P. G. Pore-lining phases and capillary breakthrough pressure of mudstone caprocks: sealing efficiency of geologic $CO_2$ storage sites. *International J. Greenhouse Gas Control* **2012**, *11*, 204−220.

(18) Mahadevan, J. Comments on the paper titled "Contact angle measurements of $CO_2$-water-quartz/calcite systems in the perspective of carbon sequestration": A case of contamination? *Int. J. Greenhouse Gas Control* **2012**, *7*, 261−262.

(19) Taherian, F.; Marcon, V.; van der Vegt, N. F. A.; Leroy, F. What is the contact angle of water on graphene? *Langmuir* **2013**, *29*, 1457−1465.

(20) Sergi, D.; Scocchi, G.; Ortona, A. Molecular dynamics simulations of the contact angle between water droplets and graphite surfaces. *Fluid Phase Equilib.* **2012**, *332*, 173−177.

(21) Scocchi, G.; Sergi, D.; D'Angelo, C.; Ortona, A. Wetting and contact-line effects for spherical and cylindrical droplets on graphene layers: A comparative molecular-dynamics investigation. *Phys. Rev. E* **2011**, *84*, 8.

(22) Halverson, J. D.; Maldarelli, C.; Couzis, A.; Koplik, J. Wetting of hydrophobic substrates by nanodroplets of aqueous trisiloxane and alkyl polyethoxylate surfactant solutions. *Chem. Eng. Sci.* **2009**, *64*, 4657−4667.

(23) Wu, C. D.; Kuo, L. M.; Lin, S. J.; Fang, T. H.; Hsieh, S. F. Effects of temperature, size of water droplets, and surface roughness on nanowetting properties investigated using molecular dynamics simulation. *Comput. Mater. Sci.* **2012**, *53*, 25−30.

(24) Holck, O.; Bauer, J.; Wittler, O.; Michel, B.; Wunderle, B. Comparative characterization of chip to epoxy interfaces by molecular modeling and contact angle determination. *Microelectron. Reliab.* **2012**, *52*, 1285−1290.

(25) Iglauer, S.; Mathew, M. S.; Bresme, F. Molecular dynamics computations of brine-$CO_2$ interfacial tensions and brine-$CO_2$-quartz contact angles and their effects on structural and residual trapping mechanisms in carbon geo-sequestration. *J. Colloid Interface Sci.* **2012**, *386*, 405−414.

(26) Solc, R.; Gerzabek, M. H.; Lischka, H.; Tunega, D. Wettability of kaolinite (001) surfaces—Molecular dynamic study. *Geoderma* **2011**, *169*, 47−54.

(27) Nielsen, L. C.; Bourg, I. C.; Sposito, G. Predicting $CO_2$-water interfacial tension under pressure and temperature conditions of geologic $CO_2$ storage. *Geochim. Cosmochim. Acta* **2012**, *81*, 28−38.

(28) Li, X.; Ross, D. A.; Trusler, J. P. M.; Maitland, G. C.; Boek, E. S. Molecular dynamics simulations of $CO_2$ and brine interfacial tension at high temperatures and pressures. *J. Phys. Chem. B* **2013**, *117*, 5647−5652.

(29) Plimpton, S. J. Fast parallel algorithms for short-range molecular dynamics. *J. Comput. Phys.* **1995**, *117*, 1−19.

(30) Plimpton, S. J. *LAMMPS Molecular Dynamics Simulator*. http://lammps.sandia.gov.

(31) Cygan, R. T.; Liang, J. J.; Kalinichev, A. G. Molecular models of hydroxide, oxyhydroxide, and clay phases and the development of a general force field. *J. Phys. Chem. B* **2004**, *108*, 1255−1266.

(32) Cygan, R. T.; Romanov, V. N.; Myshakin, E. M. Molecular simulation of carbon dioxide capture by montmorillonite using an accurate and flexible force field. *J. Phys. Chem. C* **2012**, *116*, 13079−13091.

(33) Giesting, P.; Guggenheim, S.; van Groos, A. F. K.; Busch, A. Interaction of carbon dioxide with Na-exchanged montmorillonite at pressures to 640 bar: Implications for $CO_2$ sequestration. *Int. J. Greenhouse Gas Control* **2012**, *8*, 73−81.

(34) Loring, J. S.; Schaef, H. T.; Turcu, R. V. F.; Thompson, C. J.; Miller, Q. R. S.; Martin, P. F.; Hu, J.; Hoyt, D. W.; Qafoku, O.; Ilton, E. S.; Felmy, A. R.; Rosso, K. M. In situ molecular spectroscopic evidence for $CO_2$ intercalation into montmorillonite in supercritical carbon dioxide. *Langmuir* **2012**, *28*, 7125−7128.

(35) Romanov, V. N. Evidence of irreversible $CO_2$ intercalation in montmorillonite. *Int. J. Greenhouse Gas Control* **2013**, *14*, 220−226.

(36) Brady, P. V.; Cygan, R. T.; Nagy, K. L. Molecular controls on kaolinite surface charge. *J. Colloid Interface Sci.* **1996**, *183*, 356−364.

(37) Huertas, F. J.; Chou, L.; Wollast, R. Mechanism of kaolinite dissolution at room temperature and pressure: Part 1. Surface speciation. *Geochim. Cosmochim. Acta* **1998**, *62*, 417−431.

(38) Sutheimer, S. H.; Maurice, P. A.; Zhou, Q. H. Dissolution of well and poorly crystallized kaolinites: Al speciation and effects of surface characteristics. *Am. Mineral.* **1999**, *84*, 620−628.

(39) Ganor, J.; Cama, J.; Metz, V. Surface protonation data of kaolinite-reevaluation based on dissolution experiments. *J. Colloid Interface Sci.* **2003**, *264*, 67−75.

(40) Gupta, V.; Miller, J. D. Surface force measurements at the basal planes of ordered kaolinite particles. *J. Colloid Interface Sci.* **2010**, *344*, 362−371.

(41) Neder, R. B.; Burghammer, M.; Grasl, T.; Schulz, H.; Bram, A.; Fiedler, S. Refinement of the kaolinite structure from single-crystal synchrotron data. *Clays Clay Miner.* **1999**, *47*, 487−494.

(42) Wunsch, A.; Navarre-Sitchler, A. K.; McCray, J. E. Geochemical implications of brine leakage into freshwater aquifers. *Groundwater* **2013**, *51*, 855−865.